



Enhancement of g-C₃N₄ nanosheets photocatalysis by synergistic interaction of ZnS microsphere and RGO inducing multistep charge transfer

Leqiang Shao, Deli Jiang*, Peng Xiao, Liming Zhu, Suci Meng, Min Chen*

School of Chemistry and Chemical Engineering, Jiangsu University, Zhenjiang 212013, China

ARTICLE INFO

Article history:

Received 28 March 2016

Received in revised form 17 May 2016

Accepted 22 May 2016

Available online 25 May 2016

Keywords:

g-C₃N₄

Ternary composite

Photocatalysis

Synergistic effect

Multistep charge transfer

ABSTRACT

The ternary nanocomposite of g-C₃N₄/reduced graphene oxide/ZnS (CN/RGO/ZS) has been prepared through a facile precipitation route for the first time. The as-prepared CN/RGO/ZS composite exhibit distinctly enhanced photocatalytic activities toward the degradation of Rhodamine B (about 97% after 60 min) under visible light irradiation, which was about 1.04, 1.17 and 5.38 times higher than those of CN/RGO, CN/ZS and RGO/ZS. The enhanced photocatalytic performance of RGO/CN/ZS composite arises from the synergistic effects of three components: effective charge separation, multistep transfer between CN/ZS heterojunction and RGO nanosheets, and enhanced visible-light absorption. The relative mechanism has been investigated by active species trapping and ESR analysis. This work may provide useful insights to design and construction of CN-based ternary composite photocatalysts with enhanced photocatalytic activity.

© 2016 Elsevier B.V. All rights reserved.

1. Introduction

Sunlight-driven semiconductor photocatalysis has attracted immense attention on the horizon of material science in the past few years due to its potential applications to solar energy conversion, water splitting, and environmental purification [1–4]. To effectively utilize the solar energy, development of earth-abundant, inexpensive, and visible light-driven photocatalyst has become a hot topic in photocatalysis field [5,6]. Among various photocatalysts investigated, graphitic carbon nitride (g-C₃N₄, denoted as CN) has received a lot of attention because of its visible-light driven bandgap, low toxicity, low cost, proper band edges and long-term stability [7–9]. Nevertheless, the photocatalytic efficiency of CN is still limited by the high recombination rate of photoinduced carriers and insufficient photon absorption above 450 nm, which result in low photocatalytic efficiency [10,11]. Therefore, many strategies have been proposed to improve the photocatalytic activity of CN, such as, hetero-atom doping [12–16], defect engineering [17,18], loading with noble metals (such as Ag, Au and Pd) [19–21], modifying structural morphology (such as nanosheet, mesoporous structure, nanotubes, and nanosphere) [22–26], and forming a heterojunction by integrating with other semiconductors [27–34].

Among these methods, construction of heterojunction photocatalyst is more effective since it can enable the photo-induced electrons to transfer to coupled semiconductors and efficiently facilitate the photoinduced electron–hole separation, leaving more charge carriers to anticipate in the reaction [5,35]. For example, some work has been reported by coupling CN with wide-band-gap semiconductors such as TiO₂ [36], ZnO [37,38], SrTiO₃ [39], and ZnS [40]. In these binary systems, the photo-induced electrons could transfer from the CN to the wide-band-gap semiconductors with the conduction band level lower than that of CN, thus inhibiting the recombination of the carriers and resulting in enhancement of the photocatalytic activity. However, the photocatalytic activity of binary system is still not sufficient for practical application since it usually suffers from high recombination rate of charge carriers at the interface of the two semiconductors [41]. Therefore, it is highly desirable to further improve the charge transfer dynamic of the CN-based binary photocatalytic system.

In order to further promote the charge separation and transfer of the binary system, construction of ternary system by combining conducting materials, co-catalyst, and another semiconductor has been developed [42,43]. In these multicomponent hybrid nanomaterials, multistep charge transfer was induced, which significantly leads to a remarkable enhance in the photocatalytic activity [44,45]. Specially, owing to its excellent electron mobility, graphene (GR) or reduced graphene oxide (RGO) has been widely used as a promoter to improve transfer efficiency of photogenerated charge carriers

* Corresponding author.

E-mail addresses: dlj@ujs.edu.cn (D. Jiang), chenmin3226@sina.com (M. Chen).

from the single or binary semiconductors, therefore enhancing the photocatalytic activity [46–51]. For example, Kamat and coworkers have synthesized porphyrin/ZnO/RGO hierarchical ternary photocatalysts [52]. In this hybrid system, the ternary photocatalyst exhibited significantly high photocurrent generation compared to the bare ZnO due to the multistep charge transfer on the electrode. We therefore expect that, once the multistep charge transfer was achieved in the CN-based heterojunction system by combination of RGO, the separation of the photogenerated electron–hole pairs and the photocatalytic activity of the hybrid system would be further promoted. However, so far few investigations have been reported concerning on the ternary based on the integration of CN-based binary heterojunction and GR.

In this present work, we constructed a CN/RGO/ZS ternary composite photocatalyst via a facile precipitation route. The photocatalytic activity of the samples is evaluated by the degradation of RhB under visible light irradiation. Compared with CN, ZS, CN/ZS, CN/RGO, and RGO/ZS photocatalysts, the CN/RGO/ZS ternary composite showed obviously enhanced photocatalytic activity toward the photodegradation of RhB. The enhanced photocatalytic performance of RGO/CN/ZS sample arises from the synergistic effects of three components: effective charge separation, multistep transfer between CN/ZS heterojunction and RGO nanosheets, and enhanced visible-light absorption. In addition, the mechanism of photocatalytic reaction was discussed by active species trapping and ESR analysis over the prepared CN/RGO/ZS composite photocatalyst. It is anticipated that our work could be helpful for the fabrication of CN-based ternary composite photocatalysts with efficient photocatalytic performance.

2. Experimental section

2.1. Materials

Graphite powder, hydrogen peroxide, hydrazine hydrate (Alfa Aesar), potassium permanganate (KMnO_4), hydrochloric acid (HCl), Sodium nitrate (NaNO_3), sulfuric acid, zinc nitrate hexahydrate ($\text{Zn}(\text{NO}_3)_2 \cdot 6\text{H}_2\text{O}$), nitric acid, thioacetamide (TAA), absolute ethanol and urea were purchased from Sinopharm Chemical Reagent Co., Ltd, China and were used as received without any further purification. Deionized water was used in the experiments.

2.2. Preparation of CN nanosheets

CN nanosheets were prepared according to the previously reported method [29]. In brief, 10 g of urea in a crucible with a cover under ambient pressure in air, after dried at 80°C for 24 h, the precursor was heated to 550°C at a heating rate of $2.3^\circ\text{C min}^{-1}$ in a tube furnace for 4 h in air. The resulted final light yellow powder was washed with nitric acid (0.1 mol L^{-1}) and distilled water to remove any residual alkaline species adsorbed on the sample surface, and then dried at 60°C for 24 h.

2.3. Preparation of graphite oxide and RGO sheets

Reduced graphene oxide sheets were synthesized in two steps. In the first step, Graphite oxide (GO) was synthesized from natural flake graphite by a modified Hummers method [53]. In a typical procedure, 1.0 g of graphite powder was added into cold (0°C) concentrated H_2SO_4 (100 mL) containing NaNO_3 (0.5 g) in a 500 mL flask. Under vigorous stirring, KMnO_4 (6.0 g) was added gradually and the temperature of the mixture was kept below 10°C . The reaction mixture was continually stirred for 0.5 h at a temperature below 10°C . Successively, the mixture was stirred at 35°C for 4 h until it became pasty brownish, and was diluted with deionized water (400 mL). Then, the mixture was stirred for 30 min and 15 mL

of 30% H_2O_2 was slowly added to the mixture to reduce the residual KMnO_4 , after which the color of the mixture changed to brilliant yellow. The product was then filtered and washed repeatedly with 5% HCl and distilled water. The resulted solid was centrifuged and dried at 60°C for 24 h. In the second step, 100 mg of graphite oxide was dispersed in 40 mL of water–ethylene glycol (EG) mixed solvent by ultrasonication for 1 h. Then 2.0 mL of hydrazine hydrate was slowly added in. The mixture was stirred for 10 min, and then was transferred to a 50 mL Teflonlined stainless steel autoclave and heated at 180°C for 10 h. The resultant black product was isolated and washed with deionized water and ethanol several times by centrifugation, and finally dried at 45°C in a vacuum oven.

2.4. Synthesis of CN/RGO/ZS composites

The composites were synthesized by a facile chemical bath precipitation method. Typically, CN powder (100 mg) and RGO (5 mg) were dispersed in 40 mL of distilled water by ultrasonication for 1 h, respectively. Under vigorous stirring, RGO was dispersed in CN aqueous solution by ultrasonication for 1 h. Then, $\text{Zn}(\text{NO}_3)_2$ (2.9711 g), HNO_3 (0.1 M 20 mL) and distilled water (100 mL) were added to the above mixture, which was stirred constantly, and the mixture solution was heated to 70°C , then an appropriate amount of TAA was added. After that, the solution was immersed in a 70°C water bath for 5 h. Then the reaction was quickly transferred to an ice water bath for quenching to below 5°C . The product was collected by centrifugation, washed with distilled water and absolute ethanol, and dried in an oven at 60°C in a vacuum oven. For comparison, CN/RGO, RGO/ZS, CN/ZS and ZS were also synthesized in the same way as the composite of CN/RGO/ZS with the absence of CN, RGO and ZS, respectively.

2.5. Characterization

The phase purity and crystal structure of the obtained samples were examined by X-ray diffraction (XRD, Bruker D8 Advance X-ray diffractometer) with Cu-K α radiation ($\lambda=1.5406 \text{ \AA}$). Transmission electron microscopy (TEM) characterization was carried out by a JEOL JEM-2010 (HT) operated at 200 kV. High-resolution TEM (HRTEM) images and energy-dispersive X-ray spectroscopy (EDX) were performed on a JEOL JEM-2100F transmission electron microscope at 200 kV. Surface analysis of the sample was examined by X-ray photoelectron spectroscopy (XPS) using a ESCA PHI500 spectrometer. FT-IR spectrum was performed on a Nicolet FT-IR spectrophotometer (Nexus 470, Thermo Electron Corporation) using KBr disks at room temperature. The surface areas of the photocatalysts were measured by a TriStar II 3020-BET/BJH Surface Area. UV–vis diffuse reflectance spectra (DRS) were performed on a Shimadzu UV-2450 spectrophotometer equipped with spherical diffuse reflectance accessory. The photoluminescence (PL) spectra of the photocatalysts were obtained by a Varian Cary Eclipse spectrometer with an excitation wavelength of 325 nm. The photocurrent and electrochemical impedance spectroscopy (EIS) were measured with an electrochemical analyzer (CHI 660 B Chenhua Instrument Company). The electron spin resonance (ESR) signals of spin-trapped radicals were conducted on a Bruker model ESR JES-FA200 spectrometer using spin-trap reagent DMPO in water and methanol, respectively.

2.6. Photocatalytic activity

The photocatalytic activities of the photocatalysts were tested in the degradation reaction of Rhodamine B (RhB) aqueous solution (10 mg/L) under irradiation of a 500 W tungsten light lamp. For a typical photocatalytic degradation experiment, 50 mg of photocatalyst was added into 50 mL of the above RhB solution. Prior to

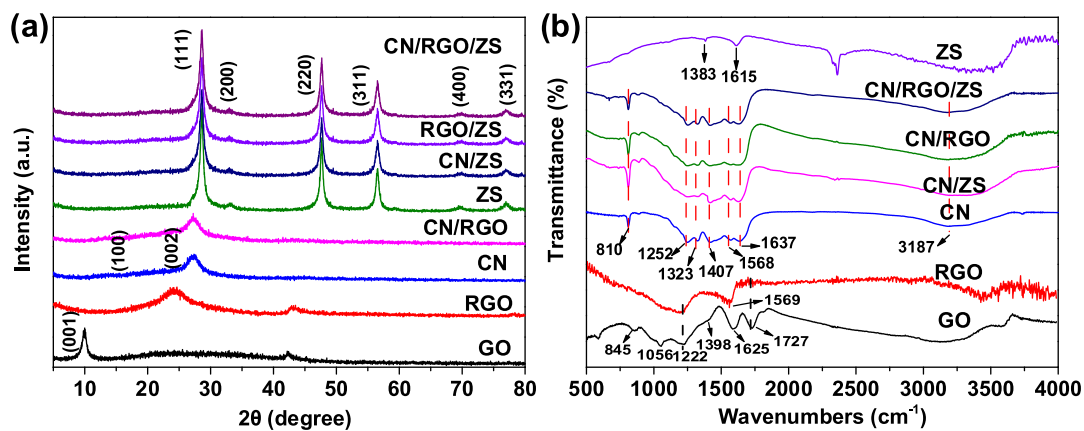


Fig. 1. (a) XRD patterns and (b) FTIR spectra of the as-prepared GO, RGO, CN, ZS, CN/ZS, CN/RGO, and CN/RGO/ZS samples.

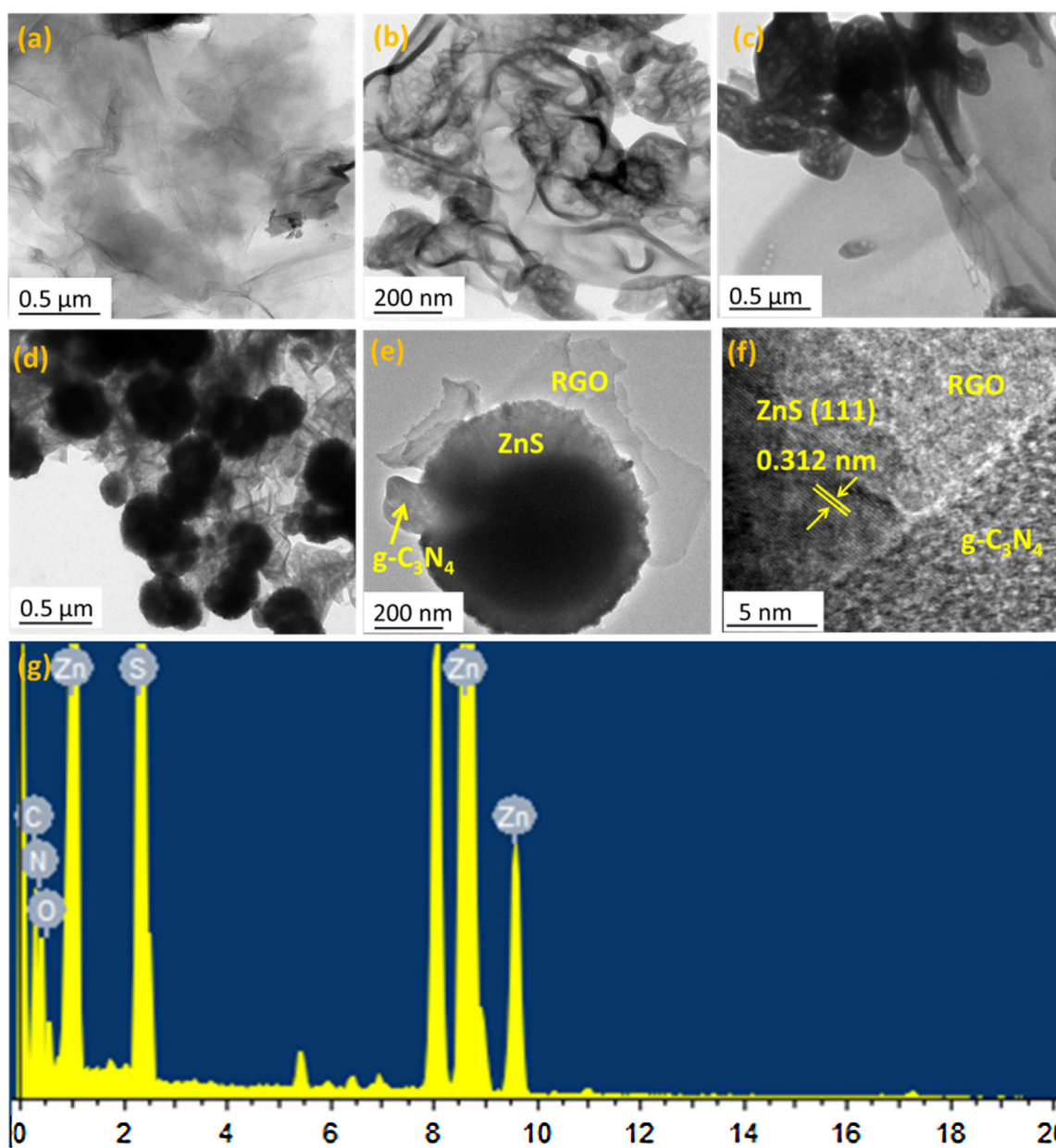


Fig. 2. Typical TEM images of (a) GO, (b) CN, (c) CN/RGO, (d) CN/ZS, (e) CN/RGO/ZS, (f) HRTEM image of CN/RGO/ZS, and (g) EDX spectra of CN/RGO/ZS.

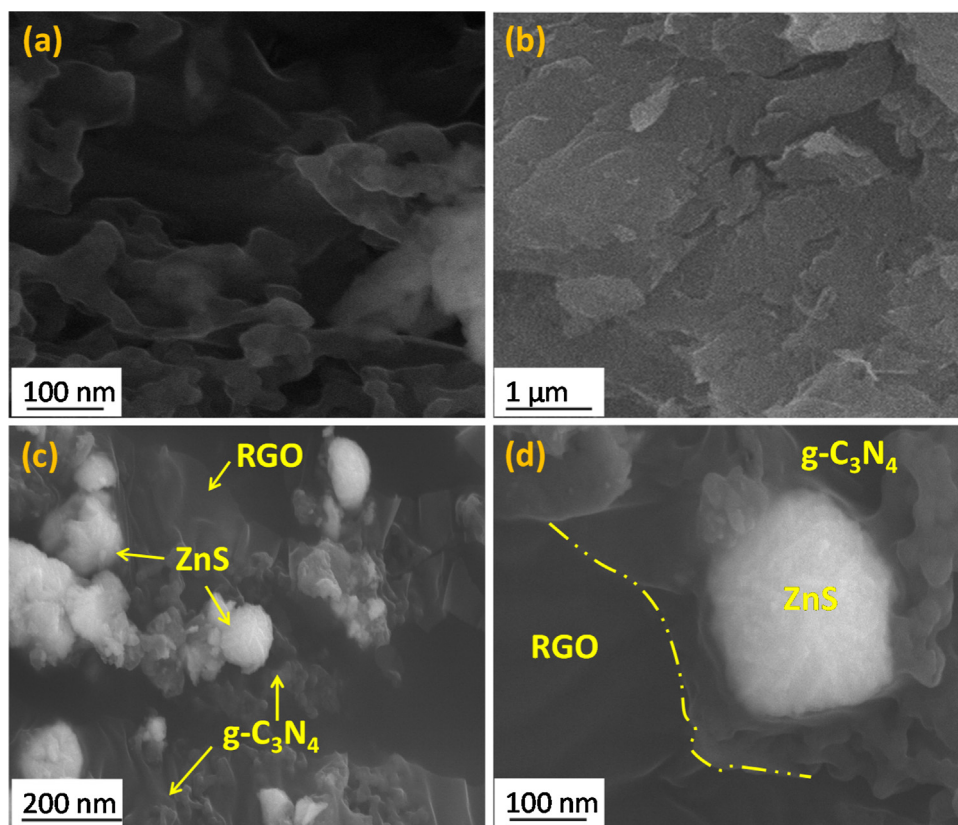


Fig. 3. SEM images of (a) CN, (b) GO and (c, d) CN/RGO/ZS.

irradiation, the suspension was magnetically stirred for 0.5 h in the dark to ensure that the RhB could reach the absorption-desorption equilibrium on the photocatalyst surface. The above suspensions were kept under constant air equilibrated conditions before and during the irradiation. During every irradiation interval, about 3 mL aliquots were collected and centrifuged to separate the photocatalysts from photodegraded dye solution. The filtrates were analyzed by a Shimadzu UV-2450 spectrophotometer and the characteristic absorption peak of RhB at 554 nm was used to determine the extent of its degradation.

2.7. Photoelectrochemical measurement

The samples photoelectrochemical properties were performed on a CHI 660B electrochemical system (Chenhua Instrument Company) using a standard three-electrode cell with a working electrode, a platinum wire counter electrode, and a saturated Ag/AgCl reference electrode. A 500 W Xe arc lamp served as a light source. The photocurrent was performed in 0.2 M Na₂SO₄ aqueous solution. The working electrodes were prepared as follows: 4 mg of the as-prepared photocatalyst was suspended in 1 mL ethanol and 20 μ L 5 wt% Nafion solution to produce a slurry. Then, 30 μ L of the resulting colloidal dispersion then dropped onto a piece of FTO slice with a fixed area of 1 cm².

3. Results and discussion

3.1. Structural and morphological analyses

Fig. 1a shows a comparison of the XRD patterns for the GO, RGO, CN, ZS, CN/ZS, CN/RGO, and CN/RGO/ZS samples recorded at diffraction angles in the range 5–80°. For the GO sample, the intense and sharp characteristic (001) diffraction peak at 10.2°, which indi-

cates the presence of oxygen-containing functional groups and the successful oxidation of original graphite into graphene oxide [54]. Compared with the pattern of GO, the strong (001) peak disappeared and a very broad diffraction peak at about 25° appeared in the diffraction patterns of RGO, confirming that GO has been flaked and reduced to graphene with a random packing and less functionalities [55,56]. The two distinct peaks at 13.0° and 27.4° in the pure CN sample can be indexed as the (100) and (002) peaks for graphitic materials, respectively, corresponding to the in-planar structural packing motif and the interlayer stacking of the aromatic system [57]. As for the pure ZS sample, all the peaks can be well indexed to the cubic phase (JCPDS 65-0309). The main diffraction peaks at 28.6°, 33.2°, 47.6°, 56.5°, 69.6°, and 76.9° correspond to the (111), (200), (220), (311), (400) and (331) crystal planes, respectively. In the CN/RGO and RGO/ZS composites, the diffraction peaks only related to CN and ZS were identified; however, peaks for RGO were not clearly visible, which was attributed to the relatively low quantity of RGO, consistent with previous reports of XRD characterization of the RGO composites [58,59]. The XRD pattern of the CN/RGO/ZS and CN/ZS composite exhibited peaks corresponding to CN and ZS microspheres, indicating the formation of a CN and ZS composite with RGO. While the characteristic peaks of CN (27.4°) and ZS (28.6°) were very close and overlap with each other.

We further analyzed the formation of GO, RGO, CN, ZS, CN/ZS, CN/RGO, and CN/RGO/ZS composites by using FTIR. As shown in Fig. 1b, for GO, the peaks at 845, 1056, 1222, 1398 and 1727 cm⁻¹ correspond to the typical stretching of C–O bonds. The peak at 1625 cm⁻¹ may be assigned to the vibration of sp² hybridized C–C bonding, O–H bending vibration of epoxide group, or O–H deformation vibration of COOH group [60–62]. The broad absorption at 3000–3700 cm⁻¹ of GO correspond to the stretching mode of –OH or the physically absorbed H₂O. After the hydrothermal reac-

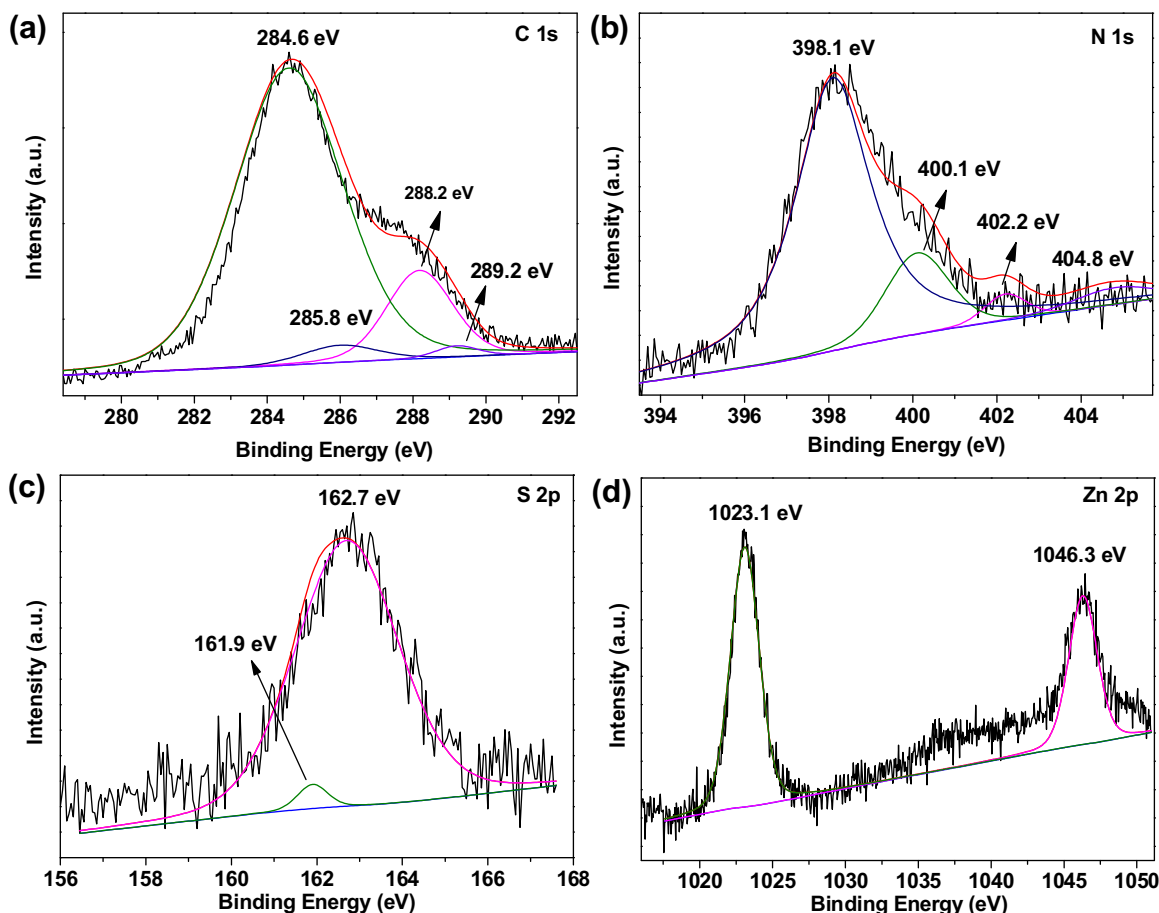


Fig. 4. XPS spectra of the CN/RGO/ZS composite: (a) C 1s, (b) N 1s, (c) S 2p and (d) Zn 2p.

tion, only weak features appear and some peaks even vanish in the spectrum of RGO, demonstrating the effective reduction of GO. Furthermore, a new absorption peak was appeared at 1569 cm^{-1} , which may be attributed to the skeletal vibration of the GR sheets [63]. The FTIR spectra of samples show the typical stretching modes of CN heterocycles in the $1200\text{--}1650\text{ cm}^{-1}$ range, the peaks at 1637 cm^{-1} are attributable to $\text{C}=\text{N}$ stretching vibration modes, while the 1252 , 1323 , 1407 and 1568 cm^{-1} can be ascribed to aromatic $\text{C}-\text{N}$ stretching vibration modes [64]. The peak at 810 cm^{-1} is related to characteristic breathing mode of s-triazine units [65]. The broad band centered at 3187 cm^{-1} can be assigned to the stretching mode of the NH bond [66]. The FTIR spectra of all the doped CN samples, the characteristic peaks of CN did not change after combination with RGO and ZS. However, the FTIR spectra of CN/RGO/ZS composite shows no obvious characteristic peaks of RGO, which was also attributed to the relatively low quantity of RGO. As for the pure ZS synthesized in the presence of TAA, the peaks at 1383 and 1615 cm^{-1} could be attributed to the TAA on the surface of ZS [41].

The morphology and microstructure of the samples are examined by TEM and high-resolution TEM (HRTEM). The TEM image of GO reveals smooth and crumpled sheets resulting from the deformation and distortion of graphite sheets (Fig. 2a). Fig. 2b shows the TEM image of the pure CN sample exhibits wrinkled lamellar and porous structure with relatively smooth surface. Meanwhile, it can be seen that the porous structure CN is dispersed on the RGO sheets (Fig. 2c). From the TEM image of CN/ZS sample (Fig. 2d), it can be found that ZS microspheres deposited on the surface of CN nanosheets. Fig. 2e shows the TEM image of the CN/RGO/ZS ternary composite, where the ZnS and RGO were formed simultaneously on

the CN. The HRTEM image of the CN/RGO/ZS composite in Fig. 2f displays distinct lattice fringes with a lattice spacing of 0.312 nm , corresponding to the lattice spacing of (111) of ZS, again confirming the formation of the CN/RGO/ZS composite. The EDX spectra of CN/RGO/ZS composite shown in Fig. 2g sufficiently indicate the existence of C, N, O, Zn, and S.

Then, the SEM images of CN, GO and CN/RGO/ZS composite are shown in Fig. 3. It can be found that the bare CN is porous and consists of many curved nanosheets with lamellar morphology, which is consistent with the TEM results (Fig. 3a). Similarly, GO has the relatively smooth and crumpled surface (Fig. 3b). In the case of the CN/RGO/ZS ternary nanocomposite, an intimate interfacial contact between CN, ZS and RGO sheets is clearly observed (Fig. 3c and d), which is beneficial for fast charge transfer across the interface. The above results manifest that the CN/RGO/ZS ternary nanocomposite has been successfully prepared by the facile precipitation route developed here.

XPS analysis was carried out to analyze the surface chemical composition and chemical states of CN/RGO/ZS. The survey scans spectrum indicates the presence of C, N, S, Zn and O element. The high resolution C 1s spectra of CN/RGO/ZS shows four peaks at 284.6 , 285.8 , 288.0 , and 289.2 eV (Fig. 4a). The peak at 284.6 eV corresponds to $\text{sp}^2\text{ C}-\text{C}$ bonds of graphitic carbon, which is also observed from RGO and those at 285.8 eV , 288.0 eV , 289.2 eV are attributed to $\text{C}-\text{OH}$ bonds, $\text{C}-\text{N}-\text{C}$ bonds, and $\text{O}-\text{C}=\text{O}$ configurations, respectively [50,67]. In the N 1s spectrum (Fig. 4b), the main signal showed occurrence of $\text{C}-\text{N}-\text{C}$ groups (398.1 eV), tertiary nitrogen $\text{N}-(\text{C})_3$ groups (400.1 eV), and $\text{N}-\text{H}$ groups (402.2 eV), respectively [40]. The weak peak at about 404.8 eV could be related to the oxidized nitrogen ($\text{N}-\text{O}$) [68,61].

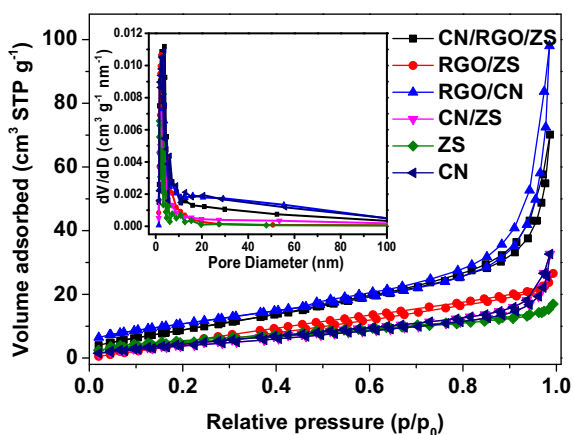


Fig. 5. Nitrogen sorption isotherm and Barrett–Joyner–Halenda (BJH) pore size distribution plot (inset) of CN, ZS, CN/ZS, RGO/ZS, CN/RGO, and CN/RGO/ZS samples.

Fig. 4c presents the high-resolution XPS spectra for S 2p which was assigned to sulfur anions in the lattice of ZS. Two peaks for S 2p are observed at 161.9 and 162.7 eV, which are assigned to S 2p_{3/2} and S 2p_{1/2}, respectively. The Zn 2p peaks located at 1023.1 and 1046.3 eV, which could be attributed to Zn 2p_{3/2} and Zn 2p_{1/2}, respectively (Fig. 4d). On the basis of the above XRD, FITR, TEM, and XPS results, it can be concluded that CN/RGO/ZS ternary nanocomposites has been successfully fabricated. Furthermore, the incorporation of RGO is benefits for the formation of intimate CN/RGO and RGO/ZS interfaces, facilitating charge transfer and separation of the photogenerated electron–hole pairs between the semiconductors, and eventually improved the photocatalytic efficiency.

3.2. N₂-Sorption studies

In order to determine the adsorption capacity toward organic pollutants, we measured the Brunauer–Emmett–Teller (BET) surface area and pore characteristic of these as-fabricated photocatalysts. Fig. 5 shows the isotherm for different samples, and the BET surface areas of the pristine CN, ZS, CN/ZS, RGO/ZS, CN/RGO, and CN/RGO/ZS are determined to be ca. 45.3, 18.7, 17.5, 31.6, 40.8, and 39.5 m²/g, respectively. It can be found that CN shows a relatively large specific surface area. Compared with CN, the BET surface areas of almost all the composite samples are slightly lower than pure CN. It may be understood that once ZS nanospheres are deposited on the surface of CN or the somewhat CN particle aggregation, they will reduce the specific surface area of the composite samples [69]. The pore-size distribution of the samples are also estimated using the Barrett–Joyner–Halenda (BJH) method from the desorption branch of the isotherm, as shown in the inset of Fig. 5, reflecting the presence of a mesoporous structure of the composites (about 2–50 nm). Compared with bare CN (3.780 nm), ZS (3.535 nm), CN/ZS (2.536 nm), CN/RGO (3.782), and RGO/ZS (2.139 nm) photocatalysts, CN/RGO/ZS (3.792 nm) has relatively bigger pore diameter. Considering the above BET results, it can be concluded that the enhanced photocatalytic activity of the samples has no direct relationship with the BET surface areas, which will be discussed below.

3.3. UV–vis diffuse reflectance spectra and band gap energy

The optical absorption properties of the photocatalysts were characterized by UV–vis absorption spectroscopy. The band gap energy of pristine CN and ZS can be calculated by the following formula: $\alpha h\nu = A(h\nu - E_g)^{n/2}$, where α , h , ν , E_g and A are absorp-

tion coefficient, Planck constant, the light frequency, the band gap, and a constant, respectively. Among them, n is determined from the type of optical transition of a semiconductor ($n=1$ for direct transition and $n=4$ for indirect transition). As shown in Fig. 6a, the steep band gap absorption edge of pure CN and ZnS are around 460 and 366 nm, respectively. The E_g of CN was found to be 2.7 eV according to a plot of $(\alpha h\nu)^{1/2}$ versus energy ($h\nu$) (Fig. 5b). Accordingly, the E_g of ZS was determined from a plot of $(\alpha h\nu)^2$ versus energy ($h\nu$) (Fig. 6b) and the band gap energy of ZS is approximately 3.4 eV. Both the band gap values of CN and ZS are well consistent with those previously reported results [12,40]. Compared to CN and ZS, CN/RGO, RGO/ZS shows more intensive absorption in the visible light region. This can be attributed to the intrinsic absorption of black colored RGO [70]. It also can be observed from the color change of the samples (see the digital pictures in Fig. 6a, inset). For the CN/RGO/ZS sample, obvious enhancement in the absorption intensity in the visible region and slight red-shift of the absorption edge are observed. The results imply that this enhanced visible light adsorption in the CN/RGO/ZS ternary hybrid could generate more photoinduced charge carriers and then lead to an enhanced photocatalytic activity.

3.4. Photocatalytic activity

The photocatalytic activities of the as-prepared samples were examined by the degradation of rhodamine B (RhB) in aqueous solution under visible light irradiation. Fig. 7a shows the variation in concentration of RhB (C/C_0) with irradiation time over different photocatalysts, where C_0 is the initial concentration of RhB and C is its concentration at time t . Prior to illumination, the suspension was magnetically stirred for 30 min in the dark to achieve the adsorption equilibrium of the RhB on the photocatalyst powders. The blank test confirms that RhB is only slightly degraded in the absence of catalysts, indicating that the photolysis of RhB can be negligible. For CN alone, the degradation ratios of RhB only reach 81% in 60 min. After 60 min visible light irradiation, the degradation rates for ZS, RGO/ZS, CN/ZS were 14%, 18%, and 83%, respectively. Notably, it can be seen that graphene exhibited an obvious influence on the photocatalytic activity of RGO/CN (about 93% after 60 min). Meanwhile, as a reference, the photocatalytic activity of physical mixture of CN, RGO, and ZS (62%) was greatly lower than CN/RGO/ZS ternary composite (97%). It clearly shows that the degradation efficiency of RhB over CN/RGO/ZS was higher than that of other photocatalysts (about 97% after 60 min). This is attributed to the fact that RGO sheets serve as electron acceptor and mediator, which can reduce the probability of electron–hole recombination, improve the separation efficiency, and therefore enhance the photocatalytic activity [63,71]. This improved charge separation efficiency induced by the RGO will be verified in the following part. Compared with other reported photocatalysts for the degradation of dyes, the as-prepared CN/RGO/ZS ternary nanocomposite shown high photocatalytic performance. For example, Hu et al. [72] has synthesized CN/GO/MoS₂ by a facile sonochemical method and more than 89.5% of RhB was degraded after 150 min. Liu et al. [73] has prepared Fe(III)/graphene/g-C₃N₄ via a simple impregnation method and more than 82% of MO was degraded after 60 min. Lü et al. [74] has prepared CN/GO/Ag by a facile hydrothermal reaction and more than 98% of MO was degraded after 6 h.

To further understand the reaction kinetics of RhB degradation, the apparent pseudo-first-order model expressed by the following formula: $\ln(C_0/C) = k_{app}t$, where k_{app} is the apparent first-order rate constant (min⁻¹), C_0 is the initial RhB concentration in aqueous solution (mg/L), C is the RhB concentration at time (mg/L). The linear relationship between $\ln(C_0/C)$ and t is shown in Fig. 7b and c. The k_{app} of CN/RGO/ZS can reach 0.05172 min⁻¹, which is larger than those of ZS (0.00238 min⁻¹), RGO/ZS (0.00300 min⁻¹),

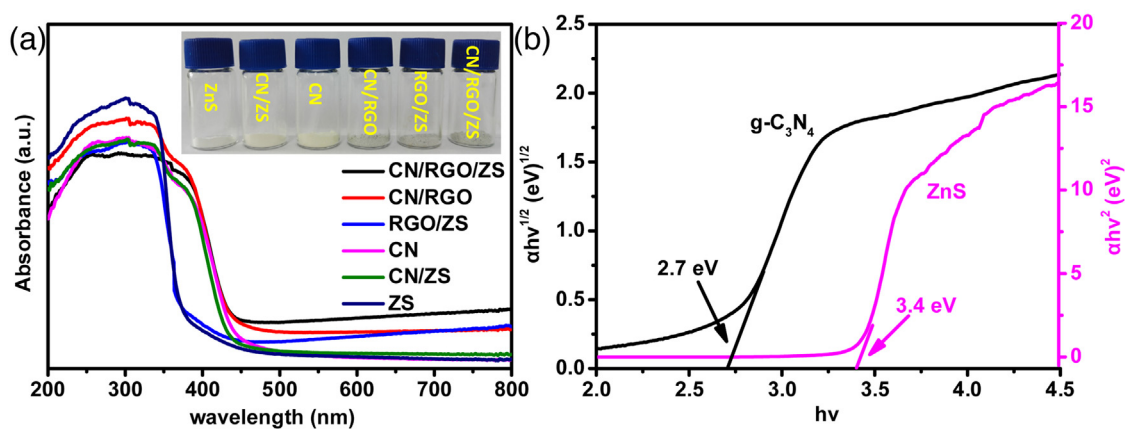


Fig. 6. (a) UV-vis diffuse reflectance spectra (DRS) of ZS, CN, CN/ZS, RGO/ZS, CN/RGO, and CN/RGO/ZS samples. (b) plot of $(\alpha hv)^{1/2}$ vs. $h\nu$ for the band gap energy of CN and ZS.

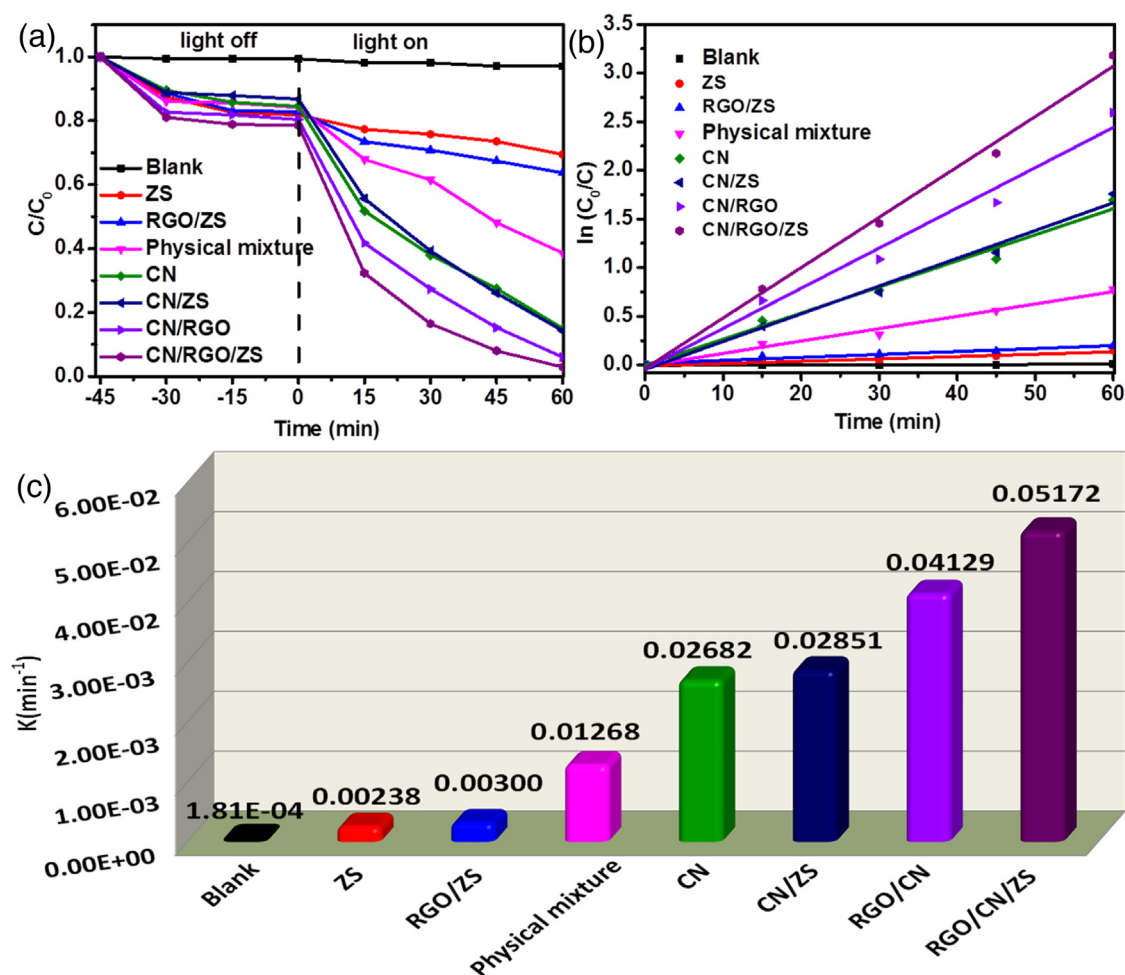


Fig. 7. (a) Photocatalytic degradation of RhB as a function of irradiation time, (b) $\ln(C/C_0)$ versus time curves of RhB degradation, and (c) values of reaction rate constants over different photocatalysts.

physical mixture (0.01268 min^{-1}), CN (0.02682 min^{-1}), RGO/CN (0.04129 min^{-1}) and CN/ZS (0.02851 min^{-1}).

3.5. Charge transfer properties

It is widely accepted that the separation efficiency of electrons and holes play a key role in the photocatalytic reaction. The higher the PL emission intensity indicates the higher the recombination

efficiency of the photogenerated carriers and the lower the photocatalytic activity [75,76]. Fig. 8a presents the PL spectra of the ZS and CN composites at an excitation wavelength of 380 and 350 nm, respectively. At room temperature, the emission band for pure ZS was centered at about 530 nm. While the emission band for pure CN was centered at about 450 nm, which was attributed to the radiative recombination process of self-trapped excitations [77]. Obviously, after coupling with ZS and RGO, the emission intensity significantly

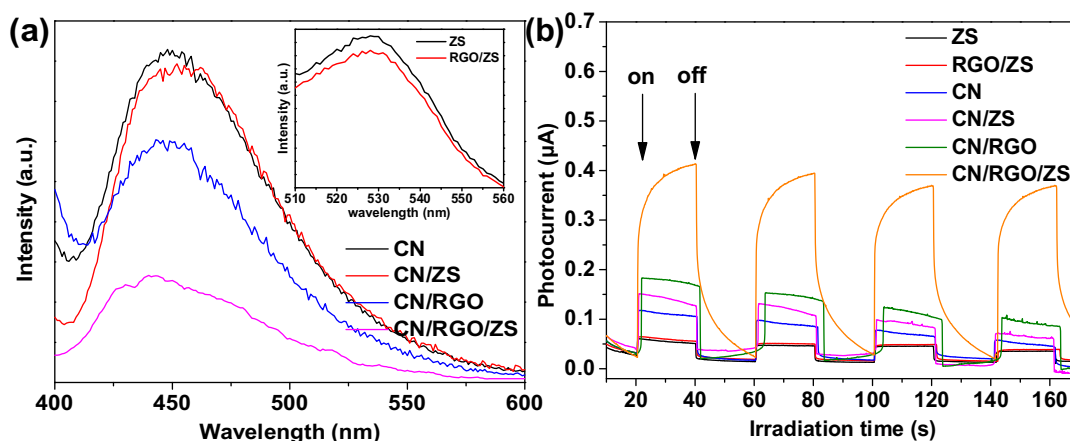


Fig. 8. (a) Photoluminescence (PL) and (b) Time-based photocurrent response plots of ZS, RGO/ZS, CN, CN/ZS, CN/RGO and CN/RGO/ZS samples.

decreased, which indicated that the binary and ternary composites exhibit slower electron-hole recombination rate compared with pure CN. Furthermore, the ternary composite (CN/RGO/ZS) showed the lowest PL intensity among the as-prepared composites, which could be attributed to the high charge-carrier mobility capability of the RGO sheets.

Photoelectrochemical measurements are often used to qualitatively study the excitation and transfer of photogenerated charge carriers in photocatalysis. The role of ZS nanospheres and RGO sheets incorporated with the CN was further investigated by measuring the transient photocurrent, which were recorded for several on-off cycles under visible light irradiation. The higher photocurrent intensity often leads to better photocatalytic activity. As shown in Fig. 8b, the photocurrent increased sharply when the light was switched on, and immediately returned to its initial state after the light source was turned off, which was repeatable [78]. This result demonstrated that most photogenerated electrons were transferred to the back contact across the samples to produce photocurrent under visible light irradiation [79]. The photogenerated current density of CN was relatively low, while CN/ZS and CN/RGO binary hybrid materials showed higher photocurrent densities. As expected, the CN/RGO/ZS exhibits the highest photocurrent intensity, indicating that the incorporation of RGO and ZS can further suppress charge recombination by improving the interfacial charge transfer under visible light irradiation. These results were consistent with photocatalytic activity measurements.

3.6. Trapping experiments

To investigate the reaction mechanism in depth, the active species formed during the reaction process are identified by a hole and free radical trapping experiment over the CN/RGO/ZS sample. Herein, the *tert*-butanol (t-BuOH) was utilized for hydroxyl radical ($\cdot\text{OH}$) scavenger, ammonium oxalate (AO) for hole (h^+) scavenger, and 1,4-benzoquinone (BQ) for superoxide radical ($\cdot\text{O}_2^-$) scavenger. As shown in Fig. 9, the photocatalytic activity of CN/RGO/ZS decreases slightly by the addition of the t-BuOH (about 77% was degraded after 60 min), but reduces greatly with the addition of AO (about 63% after 60 min) and BQ (only about 25% after 60 min). Furthermore, a N_2 purging experiment (no scavenger, N_2) indicates that the removal efficiency of RhB is obviously inhibited compared with air-equilibrated conditions (blank), implying that the dissolved O_2 primarily acted as efficient electron traps, leading to the generation of $\cdot\text{O}_2^-$, which are pivotal for the RhB degradation. Hence, these results clearly evidenced that photogenerated h^+ and $\cdot\text{O}_2^-$ are the main oxidative species for the degradation of RhB.

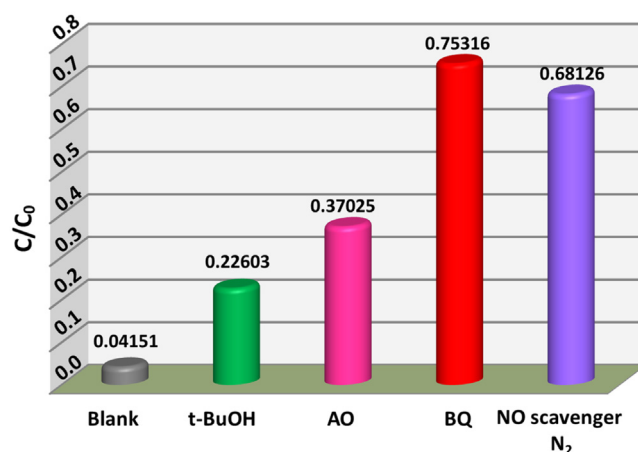


Fig. 9. Trapping experiment of the active species for the degradation of RhB.

To further detect reactive oxygen species formed over CN/RGO/ZS during the degradation process, the electron spin resonance (ESR) spin-trap technique was used. As presented in Fig. 10, there is no ESR signal in the dark. When the light is on, the characteristic quadruple peaks of the DMPO- $\cdot\text{OH}$ adducts were extremely low (Fig. 10a). However, the characteristic peaks of DMPO- $\cdot\text{O}_2^-$ can be clearly detected, further confirming the formation of $\cdot\text{O}_2^-$ during the photocatalytic process (Fig. 10b). Therefore, it is well recognized that the $\cdot\text{O}_2^-$ radicals plays an important role in the photodegradation process and the few $\cdot\text{OH}$ radicals just participate in the photocatalytic reaction.

3.7. Mechanism of enhanced photoactivity

On the basis of the above experimental results and discussion, an illustration of possible interface electron transfer behavior and the corresponding mechanism for the degradation of RhB were demonstrated in Fig. 11. Since the Fermi level of RGO (-0.08 V vs. NHE [80]) and ZS (-0.91 V vs. NHE) are more positive than the conduction-band potential of CN (-1.12 V vs. NHE). Therefore, under visible light illumination, owing to band alignment and the potential difference [81,82], the reactions might be as follows. Upon visible light excitation, electron-hole pairs are generated in the CN. The holes left in the valence band (VB) of CN are consumed in photocatalytic degradation process, while the photogenerated electrons in the CN conduction band (CB) are rapidly injected into the conduction band of the ZS due to the difference of CB edge potentials [83]. Subsequently, the electrons in the CB of ZS then could further

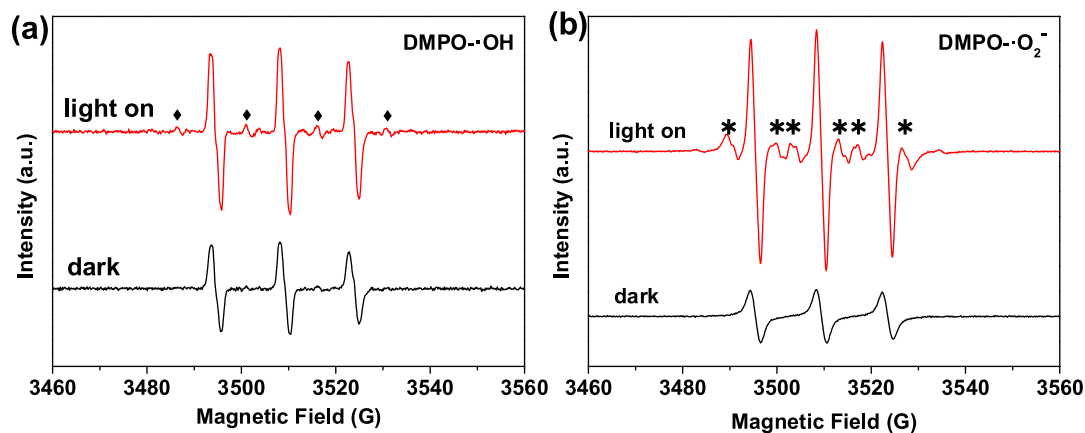


Fig. 10. DMPO spin-trapping ESR spectra for CN/RGO/ZS: (a) in aqueous dispersion for DMPO-•OH and (b) in methanol dispersion for DMPO-•O₂⁻.

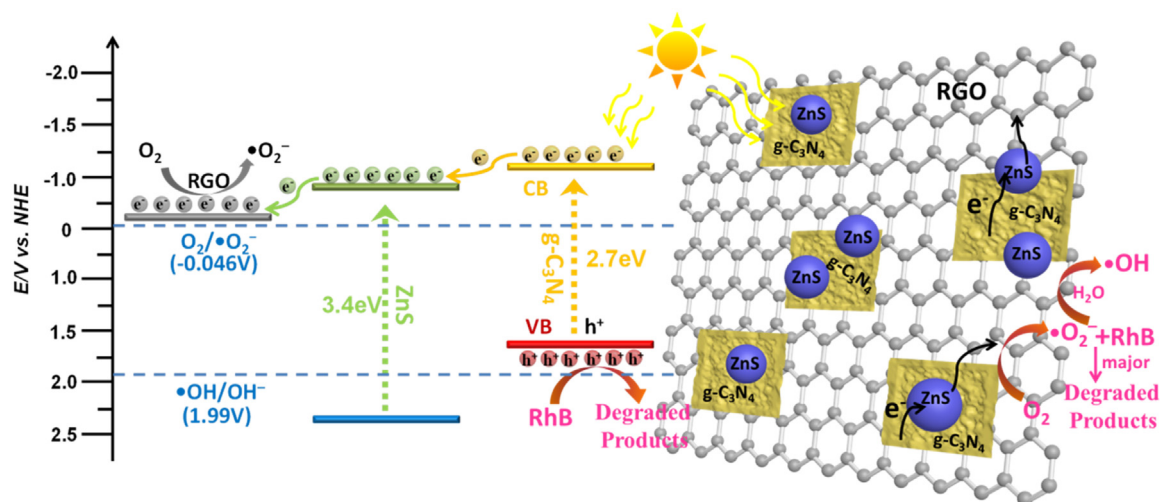


Fig. 11. Schematic illustrations of the possible charge transfer for photocatalytic degradation of RhB under visible light irradiation.

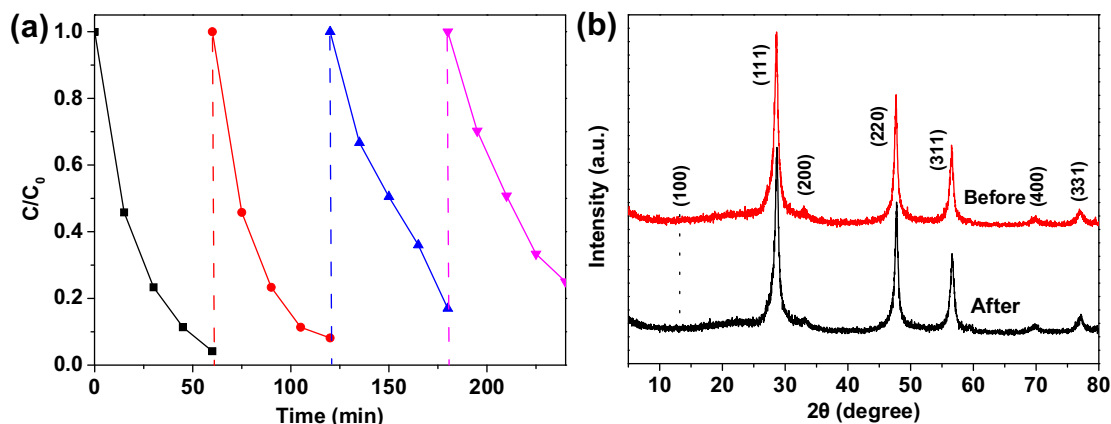


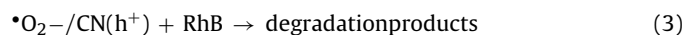
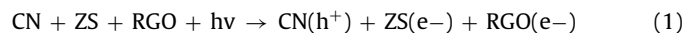
Fig. 12. (a) Cycling degradation efficiency of the RhB solution in the presence of CN/RGO/ZS sample under visible light irradiation. (b) XRD patterns of CN/RGO/ZS before and after degradation for 4 cycle reaction.

transfer to RGO, inducing a multi-steps electrons transfer instead of single-step transfer. Therefore, the charge transfer process is further promoted since ultrathin RGO with high electron mobility provide conductive pathways to facilitate the transport of photo-generated electron-hole pairs at the CN/ZS junctions. As shown in the right side of Fig. 10, the accumulated electrons in the CB of RGO can be trapped by adsorbed O₂ in water to produce •O₂⁻ radical

because the potential of RGO is more negative than the O₂/•O₂⁻ potential (-0.046 V vs. NHE). Meanwhile, the accumulated holes in the VB of CN have powerful potential to oxidize RhB directly. However, the •OH radicals cannot be formed because the VB of CN (1.58 V vs. NHE) is more negative than that of the •OH/OH• potential (1.99 V vs. NHE) [84]. Therefore, the few •OH radicals are possibly originated from the reaction of •O₂⁻ with photogenerated

ated electrons [28]. As a result, the photocatalytic activity of the CN/RGO/ZS nanocomposite can be improved because of the higher separation efficiency of photogenerated carriers.

On the basis of the related literature work and the experimental results described above [44,85], the process for the enhancement of the photocatalytic activity of CN/RGO/ZS nanocomposites can be described as follows:



3.8. Evaluation of stability

The stability and recyclability of the photocatalysts are significant factors in their practical application. The photostability of CN/RGO/ZS composite were investigated. For each recycling run, CN/RGO/ZS is collected by centrifugation, and then washed with ethanol for three times. As shown in Fig. 12a, after four recycles, the photocatalyst exhibits a slight loss of activity, suggesting that the CN/RGO/ZS is a stable photocatalyst for the degradation of RhB. This slight decrease in the photocatalytic activity may be due to the loss of the photocatalyst in the recycling process or the intrinsic unstability of ZS. As shown in Fig. 12b, XRD demonstrates that the catalyst exhibits no obvious change compared with the catalyst before the photocatalytic reaction. These results indicate that the as-prepared catalyst is stable and can be easily recycled for their practical application.

4. Conclusion

In summary, we have successfully synthesized a novel ternary hybrid photocatalyst CN/RGO/ZS with enhanced photocatalytic degradation of RhB activities under visible light irradiation. The as-prepared CN/RGO/ZS composite exhibit distinctly enhanced photocatalytic activities toward the degradation of Rhodamine B under visible light irradiation, which was about 1.04, 1.17 and 5.38 times higher than those of CN/RGO, CN/ZS and RGO/ZS. The enhanced photocatalytic performance of RGO/CN/ZS sample arises from the synergistic effects of three components: effective charge separation, multistep transfer between CN/ZS heterojunction and RGO nanosheets, and enhanced visible-light absorption. This study demonstrates that the design of CN-based composites by combining of multiple semiconductor compounds is helpful for enhancing photocatalytic activities under visible light irradiation.

Acknowledgements

This work was supported by the financial supports of National Nature Science Foundation of China (No. 21406091 and 21576121), Natural Science Foundation of Jiangsu Province (BK20140530 and BK20150482), China Postdoctoral Science Foundation (2015M570409), College Natural Science Research Program of Jiangsu Province (13KJB610003), and Key Research Plan of Zhenjiang City (GY2015031).

References

- [1] H. Tong, S. Ouyang, Y. Bi, N. Umezawa, M. Oshikiri, J.H. Ye, *Adv. Mater.* 24 (2012) 229–251.
- [2] Q.J. Xiang, J.G. Yu, M. Jaroniec, *Chem. Soc. Rev.* 41 (2012) 782–796.
- [3] B. Chen, S.H. Shen, L.J. Guo, S.S. Mao, *Chem. Rev.* 110 (2010) 6503–6570.
- [4] H.J. Li, Y. Zhou, W.G. Tu, J.H. Ye, Z.G. Zou, *Adv. Funct. Mater.* 25 (2015) 998–1013.
- [5] J.G. Li, J.X. Yu, Y.P. Low, J. Fang, X.B. Xiao, *J. Mater. Chem. A* 3 (2015) 2485–2534.
- [6] S.J. Moniz, S.A. Shevlin, D.J. Martin, Z.X. Guo, J. Tang, *Energy Environ. Sci.* 8 (2015) 731–759.
- [7] C. Wang, K. Maeda, A. Thomas, K. Takanabe, G. Xin, J.M. Carlsson, K. Domen, M. Antonietti, *Nat. Mater.* 8 (2009) 76–80.
- [8] L.T. Ma, H.Q. Fan, J. Wang, Y.W. Zhao, H.L. Tian, G.Z. Dong, *Appl. Catal. B: Environ.* 190 (2016) 93–102.
- [9] L.T. Ma, H.Q. Fan, M.M. Li, H.L. Tian, J.W. Fang, G.Z. Dong, *J. Mater. Chem. A* 3 (2015) 22404–22412.
- [10] S.W. Cao, J.G. Yu, *J. Phys. Chem. Lett.* 5 (2014) 2101–2107.
- [11] J.H. Zhang, Y. Chen, X.C. Wang, *Energy Environ. Sci.* 8 (2015) 3092–3108.
- [12] S.C. Yan, Z.S. Li, Z.G. Zou, *Langmuir* 26 (2010) 3894–3901.
- [13] G. Ma, Y.H. Lv, J. Xu, Y.F. Liu, R.Q. Zhang, Y.F. Zhu, *J. Phys. Chem. C* 116 (2012) 23485–23493.
- [14] Y.J. Zhang, T. Mori, J.H. Ye, M. Antonietti, *J. Am. Chem. Soc.* 132 (2010) 6294–6295.
- [15] P. Niu, G. Liu, H.M. Cheng, *J. Phys. Chem. C* 116 (2012) 11013–11018.
- [16] J.R. Ran, T.Y. Ma, G.P. Gao, X.W. Du, S.Z. Qiao, *Energy Environ. Sci.* 8 (2015) 3708–3717.
- [17] Q. Tay, P. Kanhere, C.F. Ng, S. Chen, S. Chakraborty, A.C.H. Huan, Z. Chen, *Chem. Mater.* 27 (2015) 4930–4933.
- [18] G. Li, A.J. Hartley, P.A. Ward, A.F. Young, T. Maschmeyer, *Mater. J. Phys. Chem. C* 119 (2015) 14938–14946.
- [19] L. Ge, C.C. Han, J. Liu, Y.F. Li, *Appl. Catal. A: Gen.* 409 (2011) 215–222.
- [20] Y. Di, X.C. Wang, A. Thomas, M. Antonietti, *ChemCatChem* 2 (2010) 834–838.
- [21] S. Bai, X.J. Wang, C.Y. Hu, M.L. Xie, J. Jiang, Y.J. Xiong, *Chem. Commun.* 50 (2014) 6094–6097.
- [22] M. Zhang, J. Xu, R.L. Zong, Y.F. Zhu, *Appl. Catal. B: Environ.* 147 (2014) 229–235.
- [23] S.E. Guo, Z.P. Deng, M.X. Li, B.J. Jiang, C.G. Tian, Q.J. Pan, H.G.F. Angew. Chem. Int. Ed. 55 (2016) 1830–1834.
- [24] J.H. Sun, J.S. Zhang, M.W. Zhang, M. Antonietti, X.Z. Fu, X.C. Wang, *Nat. Commun.* 3 (2012) 1139.
- [25] S.B. Yang, Y.J. Gong, J.S. Zhang, L. Zhan, L.L. Ma, Z.Y. Fang, R. Vajtai, X.C. Wang, P.M. Ajayan, *Adv. Mater.* 25 (2013) 2452–2456.
- [26] P. Dong, F.X. Cheng, *J. Mater. Chem. A* 3 (2015) 23642–23652.
- [27] F. Chen, J. Wei, R.J. Hou, Y. Liang, Z.L. Xie, Y.G. Zhu, X.W. Zhang, H.T. Wang, *Appl. Catal. B: Environ.* 188 (2016) 342–350.
- [28] Z.Y. Zhang, D.L. Jiang, D. Li, M.Q. He, M. Chen, *Appl. Catal. B: Environ.* 183 (2016) 113–123.
- [29] D.L. Jiang, L.L. Chen, J.J. Zhu, M. Chen, W.D. Shi, J.M. Xie, *Dalton Trans.* 42 (2013) 15726–15734.
- [30] D.L. Jiang, J. Li, C.S. Xing, Z.Y. Zhang, S.C. Meng, M. Chen, *ACS Appl. Mater. Interfaces* 7 (2015) 19234–19242.
- [31] J. Chen, S.H. Shen, P.H. Guo, M. Wang, P. Wu, X.X. Wang, L.J. Guo, *Appl. Catal. B: Environ.* 152–153 (2014) 335–341.
- [32] L.Q. Ye, J.Y. Liu, Z. Jiang, T.Y. Peng, L. Zan, *Appl. Catal. B: Environ.* 142–143 (2013) 1–7.
- [33] J.Y. Zhang, Y.H. Wang, J. Jin, J. Zhang, Z. Lin, F. Huang, J.G. Yu, *ACS Appl. Mater. Interfaces* 5 (2013) 10317–10324.
- [34] C.C. Han, L. Ge, C.F. Chen, Y.J. Li, X.L. Xiao, Y.N. Zhang, L.L. Guo, *Appl. Catal. B: Environ.* 147 (2014) 546–553.
- [35] S. Bai, J. Jiang, Q. Zhang, Y.J. Xiong, *Chem. Soc. Rev.* 44 (2015) 2893–2939.
- [36] F. Raziq, Y. Qu, X.L. Zhang, M. Humayun, J. Wu, A. Zada, H.T. Yu, X.J. Sun, L.Q. Jing, *J. Phys. Chem. C* 120 (2016) 98–107.
- [37] W. Liu, M.L. Wang, C.X. Xu, S.F. Chen, X.L. Fu, *J. Mol. Catal. A: Chem.* 368 (2013) 9–15.
- [38] D.M. Chen, K.W. Wang, D.G. Xiang, R.L. Zong, W.Q. Yao, *Appl. Catal. B Environ.* 147 (2014) 554–561.
- [39] X. Xu, G. Liu, C. Randorn, J.T.S. Irvine, *Int. J. Hydrogen Energy.* 36 (2011) 13501–13507.
- [40] F.F. Shi, L.L. Chen, C.S. Xing, D.L. Jiang, D. Li, M. Chen, *RSC Adv.* 4 (2014) 62223–62229.
- [41] S. Bai, Y.J. Xiong, *Chem. Commun.* 51 (2015) 10261–10271.
- [42] B. Chai, T.Y. Peng, J. Mao, K. Li, L. Zan, *Phys. Chem. Chem. Phys.* 14 (2012) 16745–16752.
- [43] S.R. Lingampalli, U.K. Gautam, C.N.R. Rao, *Energy Environ. Sci.* 6 (2013) 3589–3594.
- [44] S.N. Guo, Y.L. Min, J.C. Fan, Q.J. Xu, *ACS Appl. Mater. Interfaces* 8 (2016) 2928–2934.
- [45] S. Yu, S.Z. Li, X.B. Fan, J.X. Li, F. Zhan, X.B. Li, L.Z. Wu, *ChemSusChem* 8 (2015) 642–649.
- [46] Q. Xie, K. Kretschmer, G.X. Wang, *Nanoscale* 7 (2015) 13278–13292.
- [47] N. Zhang, Y.J. Xu, *CrystEngComm* 18 (2016) 24–37.
- [48] Q.J. Xiang, J.G. Yu, M. Jaroniec, *J. Am. Chem. Soc.* 134 (2012) 6575–6578.
- [49] Y. Hou, Z.H. Wen, S.M. Cui, X.R. Guo, J.H. Chen, *Adv. Mater.* 25 (2013) 6291–6297.
- [50] R.C. Pawar, V. Khare, C.S. Lee, *Dalton Trans.* 43 (2014) 12514–12527.
- [51] N. Zhang, Y.H. Zhang, X.Y. Pan, M.Q. Yang, Y.J. Xu, *J. Phys. Chem. C* 116 (2012) 18023–18031.
- [52] H. Hayashi, I.V. Lightcap, M. Tsujimoto, M. Takano, T. Umeyama, P.V. Kamat, H. Imahori, *J. Am. Chem. Soc.* 133 (2011) 7684–7687.
- [53] S. William, J.R. Hummers, R.E. Offeman, *J. Am. Chem. Soc.* 80 (1958) 1339.
- [54] J.F. Shen, B. Yan, M. Shi, H.W. Ma, N. Li, M.X. Ye, *J. Mater. Chem.* 21 (2011) 3415–3421.
- [55] C.Z. Zhu, S.J. Guo, Y.X. Fang, S.J. Dong, *ACS Nano* 4 (2010) 2429–2437.
- [56] Y.H. Zhang, N. Zhang, Z.R. Tang, Y.J. Xu, *ACS Nano* 6 (2012) 9777–9789.

- [57] K. Wang, A. Maeda, K. Thomas, G. Takanabe, J.M. Xin, K. Carlsson, M. Antonietti, *Nat. Mater.* 8 (2009) 76–80.
- [58] R.C. Pawar, D. Cho, C.S. Lee, *Curr. Appl. Phys.* 13 (2013) 50–57.
- [59] Y.L. Chen, Z.A. Hu, Y.Q. Chang, H.Q. Wang, Z.Y. Zhang, Y.Y. Yang, H.Y. Wu, *J. Phys. Chem. C* 115 (2011) 2563–2571.
- [60] Y.S. Fu, X. Wang, *Ind. Eng. Chem. Res.* 50 (2011) 7210–7218.
- [61] Q.J. Xiang, J.G. Yu, M. Jaroniec, *J. Phys. Chem. C* 115 (2011) 7355–7363.
- [62] J.F. Shen, T. Li, Y. Long, M. Shi, N. Li, M.X. Ye, *Carbon* 50 (2012) 2134–2140.
- [63] H. Zhang, X.J. Lv, Y.M. Li, Y. Wang, J.H. Li, *ACS Nano* 4 (2010) 380–386.
- [64] F. Li, J. Zhang, L.H. Shen, Y.M. Ma, W.W. Lei, Q.L. Cui, G.T. Zou, *Appl. Phys. A* 94 (2009) 387–392.
- [65] S.C. Yan, Z.S. Li, Z.G. Zou, *Langmuir* 25 (2009) 10397–10401.
- [66] M.J. Bojdys, J.O. Müller, M. Antonietti, A. Thomas, *Chem. Eur. J.* 14 (2008) 8177–8182.
- [67] P. Chen, T.Y. Xiao, Y.H. Qian, S.S. Li, S.H. Yu, *Adv. Mater.* 25 (2013) 3192–3196.
- [68] J. Zhong, J.J. Deng, B.H. Mao, T. Xie, X.H. Sun, Z.G. Mou, S.D. Wang, *Carbon* 50 (2012) 335–338.
- [69] D.L. Jiang, J.J. Zhu, M. Chen, J.M. Xie, *J. Colloid Interface Sci.* 417 (2014) 115–120.
- [70] T.F. Yeh, J.M. Syu, C. Cheng, T.H. Chang, H. Teng, *Adv. Funct. Mater.* 20 (2010) 2255–2262.
- [71] W.G. Wang, J.G. Yu, Q.J. Xiang, B. Cheng, *Appl. Catal. B: Environ.* 119 (2012) 109–116.
- [72] S.W. Hu, L.W. Yang, Y. Tian, X.L. Wei, J.W. Ding, J.X. Zhong, P.K. Chu, *J. Colloid Interface Sci.* 431 (2014) 42–49.
- [73] Q. Liu, Y. Guo, Z.H. Chen, Z.G. Zhang, X.M. Fang, *Appl. Catal. B: Environ.* 183 (2016) 231–241.
- [74] M. Lü, J.Y. Shen, J.X. Wang, Z.S. Cui, J.M. Xie, *RSC Adv.* 5 (2015) 15993–15999.
- [75] Y.Y. Bu, Z.Y. Chen, B.W. Li, *Appl. Catal. B: Environ.* 144 (2014) 622–630.
- [76] Y.J. Zhang, T. Mori, L. Niu, J.H. Ye, *Energy Environ. Sci.* 4 (2011) 4517–4521.
- [77] L. Ge, C. Han, J. Liu, *Appl. Catal. B: Environ.* 108 (2011) 100–107.
- [78] Y.Y. Bu, Z.Y. Chen, W.B. Li, *Appl. Catal. B: Environ.* 144 (2014) 622–630.
- [79] H. Xu, J. Yan, Y. Xu, Y. Song, H. Li, J. Xia, H. Wan, *Appl. Catal. B: Environ.* 129 (2013) 182–193.
- [80] L. Wang, K. Müllen Zhi, *Nano Lett.* 8 (2008) 323–327.
- [81] Y. Wang, X. Wang, M. Antonietti, *Angew. Chem. Int. Ed.* 51 (2012) 68–89.
- [82] J. Zhang, M. Zhang, R.Q. Sun, X. Wang, *Angew. Chem.* 124 (2012) 10292–10296.
- [83] R.C. Pawar, C.S. Lee, *Appl. Catal. B: Environ.* 144 (2014) 57–65.
- [84] L. Fu, W.M. Tang, L. Ji, S.F. Chen, *Chem. Eng. J.* 180 (2012) 170–177.
- [85] R.C. Pawar, V. Khare, C.S. Lee, *Dalton Trans.* 4 (2014) 12514–12527.